

## Surface analysis of corroded XV–XVI century copper coins by $\mu$ -XRF and $\mu$ -PIXE/ $\mu$ -EBS self-consistent analysis



J. Cruz<sup>a,\*</sup>, M. Manso<sup>a,b</sup>, V. Corregidor<sup>c</sup>, R.J.C. Silva<sup>d</sup>, E. Figueiredo<sup>d</sup>, M.L. Carvalho<sup>a</sup>, L.C. Alves<sup>c</sup>

<sup>a</sup> Laboratório de Instrumentação, Engenharia Biomédica e Física da Radiação (LIBPhys-UNL), Departamento de Física, Faculdade de Ciências e Tecnologia da Universidade Nova de Lisboa, Monte da Caparica, 2892-516 Caparica, Portugal

<sup>b</sup> Faculdade de Belas-Artes da Universidade de Lisboa, Largo da Academia Nacional de Belas-Artes, 1249-058 Lisboa, Portugal

<sup>c</sup> C2TN, IST-UL, Campus Tecnológico e Nuclear, E.N. 10, 2695-066 Sacavém, Portugal

<sup>d</sup> CENIMAT/13N, DCM, Faculdade de Ciências e Tecnologia da Universidade Nova de Lisboa, Monte da Caparica, 2892-516 Caparica, Portugal

### ARTICLE INFO

#### Keywords:

XRF  
PIXE  
EBS  
Coins  
Metal corrosion  
Total-IBA

### ABSTRACT

Particle Induced X-ray Emission (PIXE) and X-ray Fluorescence (XRF) are nowadays routinely used for analysing historical coins. However, its characterization, especially in the presence of a superficial chemically altered layer (corrosion), is difficult due to its layered structure which cannot be probed using these two techniques in the general case. Elastic backscattering (both Rutherford and non-Rutherford) spectrometry is commonly used to determine depth profiles but by its own it is insufficient to unveil these complex structures. Using a PIXE detector and a particle detector recording simultaneously it is possible to perform a self-consistent analysis to obtain results about concentration variation of different elements along depth. In the present work this method was tested for two Portuguese centenary copper-based coins, and XRF was used to complement PIXE information. It is shown that elemental depth profiles with the evaluation of the superficial altered layer can be clearly solved providing relevant results about corrosion extension and composition.

### 1. Introduction

The study of corrosion products in cultural heritage metallic artefacts provide important information about the degradation mechanisms that occurred or are still occurring and about their extension. These studies improve the knowledge of the state of preservation of an object and can become base guidelines for conservation/restoration procedures.

Since sampling is not always compatible with the preservation of ancient or historical artefacts, techniques like XRF (X-ray Fluorescence) mainly, but also PIXE (Particle Induced X-ray Emission) have become recurrent elemental characterization techniques used in the past years [1,2]. They are non-destructive and the analysis can be undertaken without physical contact with the artefact's surface. Additionally, they are multi-elemental techniques and quantitative results with sensitivities down to the  $\mu\text{g/g}$  level can be obtained without requiring certified reference materials. In microbeam mode ( $\mu$ -XRF,  $\mu$ -PIXE), high resolution 2D elemental mappings of content distribution at a small surface area can also be obtained.

When using only these two techniques on the surface of an object, results relate mainly to the first tenths of micrometres of depth, which frequently relates only to the corrosion layer since corrosion can extend to a depth of hundreds of microns [3]. Since it is extremely hard to derive elemental depth distributions from XRF or PIXE data alone using the X-ray L-line/K-line ratio for some elements [4,5] due to limited depth range (determined by the energies of the L and K characteristic lines) and corrosion heterogeneities through depth (corrosion can exist in chemically differentiated multilayers), this approach is mined by large uncertainties.

To overcome these constrains, and to better complement X-ray data, Rutherford (RBS) and non-Rutherford (EBS) elastic backscattering have been combined in previous studies [6–11] with PIXE for the determination of light elements and to get information about the superficial layered structure. In some of these studies [6,7], the data analysis was performed step by step by combining X-ray spectrum fitting and backscattered particle spectrum simulation, which is time consuming and not automatically self-consistent; in other studies [8–11] the “Total IBA” concept [11] was applied to EBS/PIXE spectra taken simulta-

\* Corresponding author.

E-mail address: [jdc@fct.unl.pt](mailto:jdc@fct.unl.pt) (J. Cruz).

neously with the resulting information fitted self-consistently by using the DataFurnace code [12]; in particular, J. Cruz et al. [10] extracted elemental depth profiles for corroded layers for two 15th–16th century Portuguese coins where a large number of minor and trace elements were detected. The authors mention that the proposed depth distribution for these elements had to be taken with some care, since small variations on these distributions usually do not contribute significantly to the variation of global EBS spectra resulting in an inevitable uncertainty in terms of depth distributions.

A way to reduce the uncertainty of the experimental method employed in [10] is to establish which elements are most likely part of the metal bulk and which are most likely external contaminations that are accumulated on the coin's surface and can take part of the corrosion development. There are several elements that are used in archaeometallurgical provenance studies whose concentrations are predominantly governed by ore mineralogy/composition and closely related to the smelting technology from which a metal was extracted, as well as others that can mainly be related to soil or aerial contaminations. A variety of metals have been and are still used to fabricate coins, but in this work, the interest is limited to copper.

Pernicka [13,14] classified the behaviour of trace elements during the smelting operations of oxide and sulphide ores to obtain copper. The elements silver (Ag), gold (Au), bismuth (Bi), iridium (Ir), nickel (Ni), osmium (Os), palladium (Pd), platinum (Pt), rhodium (Rh), ruthenium (Ru), cadmium (Cd), mercury (Hg) and thallium (Tl) were classified as ore fingerprints, i.e. are preferentially incorporated in metal from its original ore, and the elements arsenic (As), cobalt (Co), indium (In), lead [Pb (< ~ 5%)], rhenium (Re), antimony (Sb), tin [Sn (< ~ 1%)], selenium (Se), tellurium (Te) and zinc [Zn (< ~ 2%)] were classified either as ore fingerprints or production technology by-products, i.e., elements that can also be present due to metallurgical practices and choices.

Iron (Fe) and sulphur (S) are elements that can be incorporated in the metal surface and become part of corrosion layers since these elements are common in soil and atmosphere. However, they can also be part of metal bulk due to incomplete separation during smelting operations (most copper ores contain Fe and S as major elements) and can thus also be considered as ore fingerprints. On the other hand, oxygen (O), carbon (C) and chlorine (Cl) are elements strongly related to corrosion mechanisms and structures.

The qualitative evaluation by Pernicka can be complemented from published data on identical copper coins bulk's composition that show the profitable use of trace elements such as Ni, As, Ag, Sn, Sb, Pb, Au and Zn for the distinction of different mints. Guerra [15] and Magro et al. [16] studied about 300 copper coins minted in Portugal during the 15th to the 16th centuries by fast neutrons cyclotron activation and showed that coins minted by consecutive kings are well differentiated and defined, meaning that stocked or reused copper was kept to a minimum. The use of different stocks with different trace element fingerprints through time is well understood by coeval documents that describe the different copper provenances: Portugal (Alentejo region), Germany (copper that came through the commercial circuit of Flanders), North Africa (in principle from Ofrane mine), and Spain [16].

In the present work it is shown that the use of  $\mu$ -XRF to identify and quantify trace elements, proposed as alloy constituents, is profitably used as input in the self-consistent PIXE/EBS analysis thus reducing a source of uncertainty reported in [10]. XRF is an adequate technique because it has a swift setup, short acquisition times and can probe deeper into the coin's bulk as compared to PIXE and EBS, giving more robust information about the copper matrix composition. This technique is nonetheless a surface technique and the inevitable superficial copper altered layer bias the results measured by this technique. This was dealt with by measuring with  $\mu$ -XRF different regions and from here to understand how the surface-altered layer influenced the results, proposing thus a minimum-bias alloy composition.

## 2. Materials and methods

### 2.1. Studied coins

The studied copper coins belong to the Portuguese second dynasty: a Real Preto (1.35 g;  $\varnothing$  22 mm) minted during D. Duarte reign (1391 to 1438, king since 1433) (Fig. 1); and a 2 Reais (3.26 g;  $\varnothing$  25 mm) minted during D. António reign (1531–1595, king from 1580 to 1581) (Fig. 2).

The coins were in fine state of preservation, and their surfaces presented a rather uniform colour, ranging from dark brown to black. Both coins presented a corrosion layer of unknown thickness and composition. These coins belong to a private collection and due to their rarity, they were available for analysis only for a limited period.

The coins were cleaned with alcohol and a soft tissue before the measurements and their surfaces were optically inspected with an Olympus SZX9 stereo microscope.

### 2.2. $\mu$ -XRF

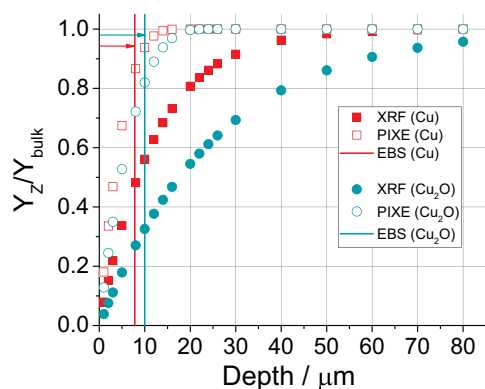
XRF measurements were performed with a Bruker's M4 Tornado  $\mu$ -XRF spectrometer. The excitation of fluorescence radiation is performed by a Rh ( $E_{K\alpha} = 20.216$  keV) anode side window X-ray tube with a polycapillary lens offering a spot size down to 25  $\mu$ m combined with high excitation intensity. Detection of fluorescence radiation was performed by an energy-dispersive silicon drift detector (SDD) with 30 mm<sup>2</sup> sensitive area and energy resolution of 142 eV for Mn-K $\alpha$ . The X-ray generator was operated at 50 kV and 300  $\mu$ A for 200 s with a composition of filters (100  $\mu$ m Al/50  $\mu$ m Ti) between the primary beam and the sample, to reduce the background contribution from the X-ray tube. Analyses were carried out directly on the coin which was placed on the  $\mu$ -XRF platform under 20 mbar vacuum conditions. The small beam dimension gives the ability to distinguish surface heterogeneities down to the tens of micrometre size. The X-ray tube and the SDD detector are placed at 20° to the sample normal. Spectra acquisition and



Fig. 1. Photograph of the studied Real Preto (king D. Duarte I). Left image: Obverse; right image: reverse.



Fig. 2. Photograph of the studied 2 Reais (D. António). Left image: Obverse; right image: reverse.



**Fig. 3.** Simulated XRF and PIXE relative yields for the copper X-ray  $K_{\alpha}$ -line yield as a function of depth for pure copper (red points) and for cuprite ( $\text{Cu}_2\text{O}$ ) (green points). The depth probed by EBS is indicated by the vertical lines, red for copper and green for cuprite. (For interpretation of the references to colour in this figure legend, the reader is referred to the web version of this article.)

2D elemental maps evaluation were carried out using the Esprit software from Bruker.

In terms of sensitivity, for XRF the lowest limit of detection (LOD) can be as low as a few  $\mu\text{g/g}$ . The accuracy of the measurements depends on the counting statistics and fitting calculation.

### 2.3. PIXE and EBS

PIXE and EBS spectra were obtained simultaneously under vacuum conditions ( $5 \times 10^{-6}$  mbar) at the microprobe beam line of the 2.5 MV Van de Graaff Accelerator of the CTN/IST (Lisbon, Portugal) [17] using a 2.0 MeV proton beam at normal incidence. The beam dimensions,  $3 \times 4 \mu\text{m}^2$ , give the ability to distinguish surface inhomogeneities down to the micrometre size.

The PIXE spectra were collected using an 8  $\mu\text{m}$  thick Be windowed Si(Li) detector with 145 eV resolution placed at  $135^\circ$  to the beam direction. It was operated with a 50  $\mu\text{m}$  thick Mylar foil in order to protect the detector from backscattered protons.

The EBS spectra were collected with a 200  $\text{mm}^2$  PIPS detector with 30 keV resolution in Cornell geometry placed at  $140^\circ$  to the beam direction.

Microprobe operation and basic data manipulation, including X-ray surface elemental distribution mapping, was achieved through the OMDAQ software code [18]. Beam scans over the surface of the samples can range up to  $2640 \times 2640 \mu\text{m}^2$ . In selected points of interest, PIXE spectra evaluation and quantification was done with the GUPIXWIN [19] code, assuming a bulk sample. The results, which include the elemental concentration and the peak area of each X-ray line, were used as input in the DataFurnace code [12] to fit the EBS spectra, thus providing a self-consistent elemental depth profiles for each selected point of interest. This procedure was implemented assuming local search fitting, and some constraints were imposed depending on the studied coin (see details in next section). The beam straggling was calculated assuming Chu correction with Tschälar effect.

In terms of sensitivity, for PIXE the lowest limit of detection (LOD) can be as low as a few  $\mu\text{g/g}$ . The accuracy of the measurements was only dependent on the counting statistics and fit uncertainty. So, in general, major element concentration is obtained with accuracy below 0.2%. For the minor elements, this accuracy degrades, being about 5% for absolute concentrations around 0.1% and about 20% for trace elements. For EBS, the LOD is around 3% and the depth resolution of concentration profiles is estimated to be around 10 nm.

For these experimental conditions it is relevant to calculate the depth probed by each of the three techniques (XRF, PIXE, EBS) and for two kind of samples: pure copper and cuprite ( $\text{Cu}_2\text{O}$ ) which is a

common copper oxide. For XRF the relative yield for the copper X-ray  $K_{\alpha}$ -line as a function of depth is calculated by applying the Lambert-Beer law to the incoming 20.2 keV Rh X-ray photon and to the emitted copper X-ray photon of 8.04 keV:

$$\frac{Y_z}{Y_{\text{Bulk}}} = 1 - \exp\left[-\mu(E = 20 \text{ keV}) \times \frac{z}{\cos \theta}\right] \times \exp\left[-\mu(E = 8 \text{ keV}) \times \frac{z}{\cos \theta}\right]$$

where  $z$  is the depth of interaction in the sample,  $\mu$  is the linear attenuation coefficient and  $\theta = 20^\circ$  is the angle of the X-ray tube and the angle of the SDD X-ray detector with respect to the sample normal. For PIXE, the same yield was computed with the GUPIXWIN code. For EBS, the depth probed was simulated with DataFurnace code. Fig. 3 shows the results from these calculations, in red for pure copper and in green for cuprite. This plot shows that EBS and PIXE probe essentially the same depth ( $\sim 8 \mu\text{m}$  for pure copper and  $\sim 10 \mu\text{m}$  for cuprite), while XRF probes considerably deeper, as expected.

## 3. Results and discussion

### 3.1. $\mu$ -XRF results

XRF analyses were performed on both sides of each coin and for each side an elemental surface mapping was obtained.

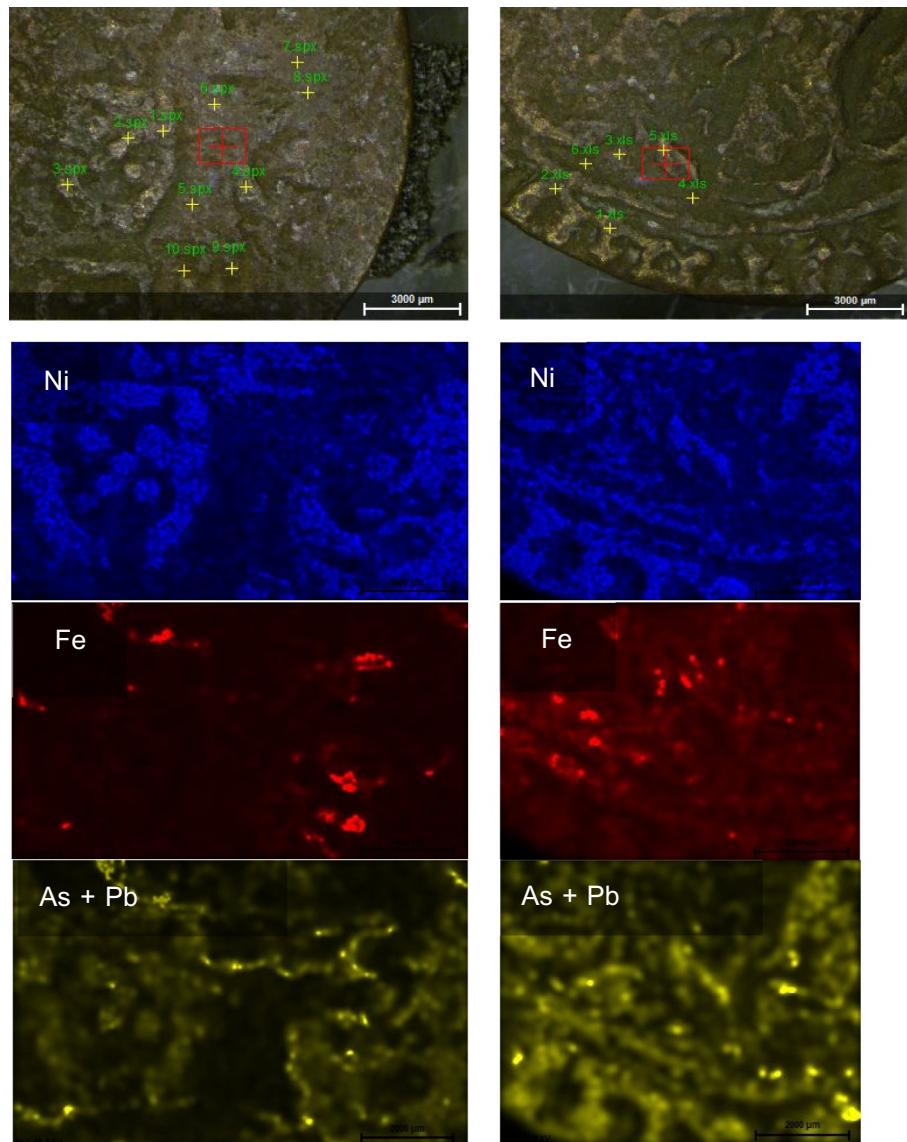
#### 3.1.1. Real Preto

Fig. 4 shows the photos of the two areas scanned with the Tornado setup alongside with the Ni- $K_{\alpha}$  (7.48 keV), Fe- $K_{\alpha}$  (6.40 keV) and As- $K_{\alpha}$  (10.543 keV) + Pb-L $_{\alpha}$  (10.551 keV) surface maps [ $9.7 \times 6.2 \text{ mm}^2$  (obverse) and  $7.6 \times 6.1 \text{ mm}^2$  (reverse)]. For these maps, more vivid colour represents higher elemental content. A total of 16 points (10 on the obverse and 6 on the reverse sides of the coin, marked in Fig. 4 with yellow crosses) with a low iron signal were selected for quantitative point analysis. From Fig. 4, it is observed that iron is agglomerated in millimetre sized areas mainly in low relief areas, and therefore the iron can be interpreted as a result of an external origin, namely dirt accumulation. These high Fe regions are therefore of little interest to perform elemental analysis since they will show high influence from external elements.

The elemental analysis performed in the 16 spots with low amount of Fe is therefore more adequate to deliver pertinent information about the identity and quantity the trace elements present in the copper matrix. Results are summarized in Table 1. All 16 points revealed the presence of trace amounts of iron, cobalt, nickel, zinc, arsenic, silver, tin, antimony and lead. Bismuth was detected and quantified only for 8 of the 16 points. Elements lighter than iron are not detected due to the low ionizing cross sections for the incident X-ray beam and absorption in the filter.

Taking into account that corrosion phenomena leads to selective depletion of some elements in relation to others, and being copper an element that has shown to be preferentially depleted in relation to Sn and As in normal corrosion conditions [20–22] the correlation of the minor elements in relation to copper was tested (Fig. 5). Results showed that As and Ni have a clear negative correlation to Cu, and that most of the other elements show neither positive nor negative strong correlation tendencies regarding Cu composition. Exceptions are for Fe and Pb that show dispersed composition records. This can be so because Fe in the analyses is a contribution from the alloy and surface contamination. Regarding Pb, this element is insoluble in copper, leading to its dispersion in the copper microstructure as small as globules of micrometre size. The resulting microstructure is thus heterogeneous (at micrometre scale) and this may affect the spot analysis results. Other elements, such as Ag, Co, Bi are also very insoluble in copper, but probably their rather smaller content in the alloy ( $< 0.1\%$ ) does not result in strong heterogeneities to be detected by the spot XRF analysis.

Copper does form solid solutions with Sn, Sb, As and Ni. The tendency for negative correlations of As and Ni in relation to Cu



**Fig. 4.** Real Preto (D. Duarte): Photographs and Ni-K $\alpha$ , Fe-K $\alpha$  and As-K $\alpha$  + Pb-L $\alpha$  surface maps [9.7 × 6.2 mm<sup>2</sup> (obverse) and 7.6 × 6.1 mm<sup>2</sup> (reverse)]. More vivid colour represents higher elemental concentration. In the photographs yellow crosses indicate the locations where μ-XRF point analysis was performed. (For interpretation of the references to colour in this figure legend, the reader is referred to the web version of this article.)

**Table 1**  
Real Preto: Elemental concentrations (wt%) obtained by XRF. See text for details.

#	Cu	As	Ag	Sn	Pb	Fe	Ni	Co	Zn	Sb	Bi
Obverse side											
1	98.80	0.119	0.094	0.059	0.188	0.023	0.330	0.026	0.01	0.348	0.006
2	97.20	0.696	0.101	0.076	0.386	0.011	1.037	0.045	0.01	0.426	0.010
3	97.92	0.260	0.108	0.059	0.520	0.046	0.612	0.071	0.01	0.386	0.007
4	98.32	0.248	0.076	0.065	0.276	0.045	0.578	0.063	0.01	0.318	n.d.
5	98.87	0.133	0.108	0.066	0.314	0.037	0.114	0.037	0.01	0.301	0.014
6	98.52	0.192	0.100	0.054	0.394	0.042	0.291	0.025	0.01	0.364	0.011
7	98.45	0.242	0.100	0.054	0.165	0.026	0.554	0.035	0.01	0.355	0.009
8	98.55	0.198	0.083	0.062	0.160	0.034	0.510	0.035	0.01	0.352	0.006
9	97.99	0.321	0.092	n.d.	0.324	0.028	0.803	0.055	0.01	0.376	n.d.
10	98.01	0.411	0.075	0.058	0.469	0.365	0.253	0.054	0.01	0.301	n.d.
Reverse side											
1	97.55	0.408	0.095	0.058	0.257	0.124	1.009	0.097	0.01	0.394	n.d.
2	97.43	0.479	0.084	0.062	0.273	0.161	1.020	0.100	0.01	0.377	0.005
3	97.00	0.586	0.084	0.070	1.067	0.058	0.725	0.041	0.00	0.367	n.d.
4	98.45	0.287	0.096	0.054	0.154	0.054	0.484	0.024	0.01	0.387	n.d.
5	96.59	0.832	0.087	0.052	0.481	0.020	1.446	0.059	0.01	0.422	n.d.
6	98.70	0.121	0.106	0.057	0.352	0.201	0.143	0.025	0.01	0.278	n.d.

n.d. = not detected.

composition, and to a smaller extent Sb in relation to Cu (Sn is present in very small amounts < 0.1% which does not allow the observation of any tendency) can be related to the original copper solid solution composition, that in turn can show heterogeneities at the microscale (e.g. coring that occurs during solidification). Otherwise, it can be a result of the preferential depletion of Cu with respect to the other elements during corrosion phenomena. These possibilities concern only natural occurrences. However, the fact that nickel and arsenic are preferentially located in the high relief regions may indicate an intentional man-made process (e.g., polishing, coating). The absence of iron precludes dirt as the origin for this process.

Taking into consideration the results obtained by the XRF spot analysis one can propose that the alloy composition of the coin must be close to (in units of wt%):  $98.8 \pm 0.2$  copper,  $0.13 \pm 0.02$  nickel,  $0.127 \pm 0.008$  arsenic,  $0.12 \pm 0.12$  iron,  $0.107 \pm 0.002$  silver,

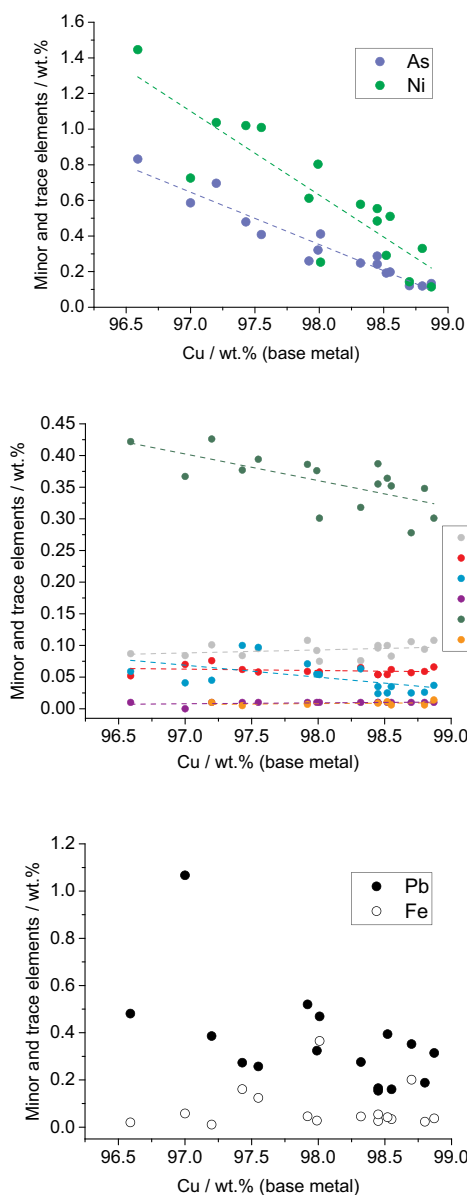


Fig. 5. Real Preto (D. Duarte): Relations among trace elements and copper concentrations obtained by XRF spot analysis in Real Preto (D. Duarte) coin: (top) negative correlation between (As and Ni) minor elements and Cu; (middle) absence of strong negative or positive correlation between (Ag, Sn, Co, Zn, Sb and Bi) minor elements and Cu; (bottom) dispersed composition records of (Pb and Fe) minor elements.

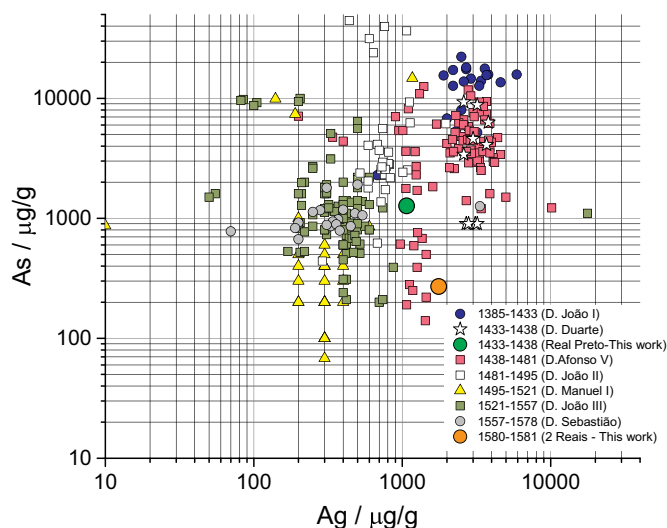


Fig. 6. Evolution of the As vs Ag composition (in µg/g) of copper coins minted in Portugal from 1385 to 1578 (Refs. [15,16]), and comparison with the Real Preto and 2 Reais results.

$0.061 \pm 0.007$  tin,  $0.29 \pm 0.02$  antimony,  $0.33 \pm 0.03$  lead,  $0.031 \pm 0.009$  cobalt,  $0.010$  zinc.

It corresponds to the concentrations obtained by averaging data from points with lower nickel content (< 0.15 wt%), which from Fig. 5 is seen to be located at the higher copper content region.

Taking into consideration this compositional hypothesis and comparing it to coeval coins (1433–1438 - D. Duarte) compositions [15,16] it is possible to conclude that, as shown in Fig. 6, the As concentration is in the same range as the coeval coins (900–9300 µg/g) but the Ag concentration is smaller than the concentration determined for coins in previous analysis (2600–3800 µg/g). Thus, if silver concentration is to be used as a strong marker for the minting place or period attribution, clearly the present analysis possesses some problems.

If other elements are considered, such as Sn, Sb, Pb or Ni (Fig. 7), a tendency can be found to higher amounts of Sb and comparable amounts of Sn, Pb and Ni of the present analysis when compared to coeval coins. These results by their own show that either there is an interference of corrosion layers in the present analysis that inhibits a good attribution based on minor/trace elements, or that the analysed

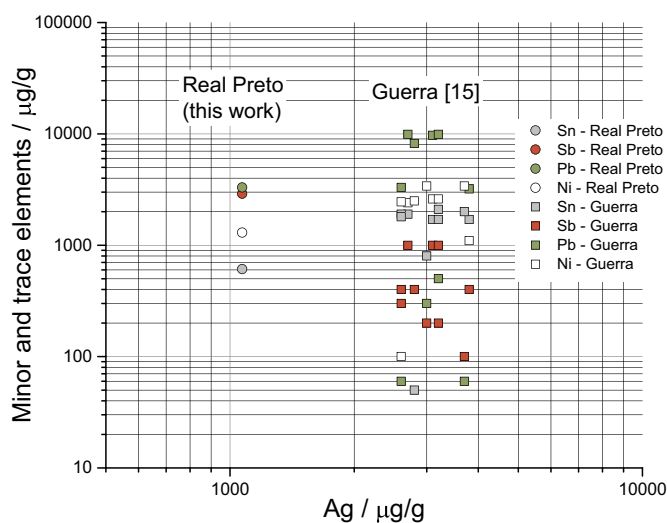
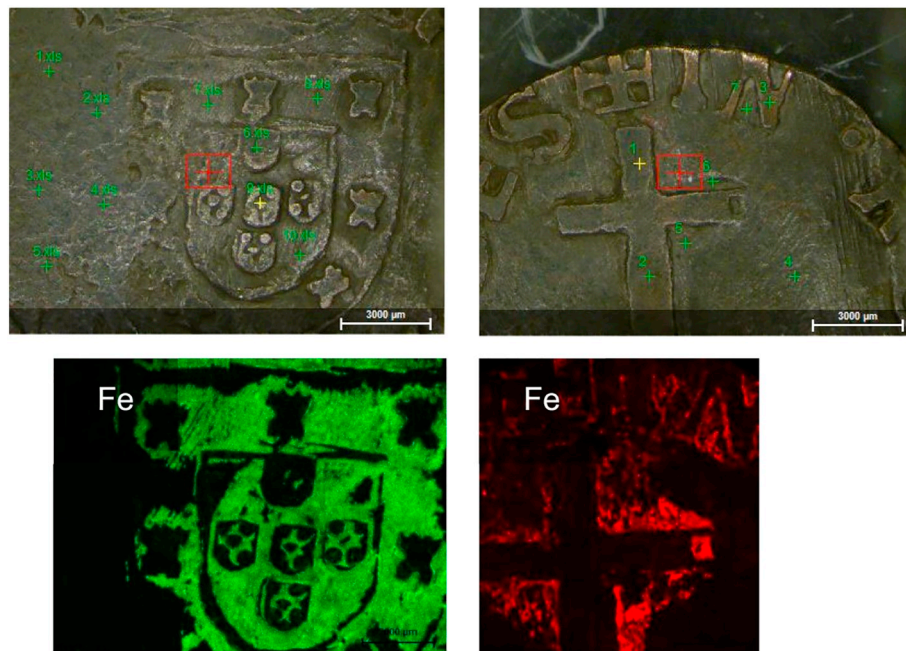


Fig. 7. Evolution of the Sn, Sb, Pb and Ni vs Ag composition (in µg/g) of copper coins minted in Portugal in the reign of D. Duarte [15], and comparison with the Real Preto results.



**Fig. 8.** 2 Reais (D. António): Photographs and Fe-K $\alpha$  surface maps [7.6 × 6.1 mm<sup>2</sup> (obverse) and 7.2 × 7.7 mm<sup>2</sup> (reverse)]. More vivid colour represents higher elemental concentration. The photographs indicate the locations where  $\mu$ -XRF point analysis was performed.

coin does not possess an impurity pattern similar to those minted during D. Duarte's reign and previously determined.

3.1.2. 2 Reais

Fig. 8 shows the photos of the two areas scanned with the  $\mu$ -XRF setup alongside with the Fe-K $\alpha$  (6.40 keV) surface maps [7.6 × 6.1 mm<sup>2</sup> (obverse) and 7.2 × 7.7 mm<sup>2</sup> (reverse)]. A total of 17 points (10 on the obverse and 7 on the reverse sides of the coin) were analysed. The elemental information gathered from this analysis is summarized in Table 2. All 17 points revealed the presence of trace amounts of Ag, Sn and Pb (Ti, Cr, Mn, Co, Zn, As, Sb and Bi were detected and quantified only at some points). In comparison to the previous coin analysed, (Real Preto), this coin shows absence of Ni (n.d.) and generally lower amounts of As (< 0.14%). Fe was detected everywhere in a wide range of concentrations having in some spots very high contents, above 4%, mainly in the low reliefs, and can thus be related to dirt and corrosion

accumulation. For this coin, point analysis was performed in low Fe content regions (as happened to the Real Preto) and in medium/high Fe content regions in order to test the influence from external elements. Considering the analyses with the lowest Fe contents and Cu > 99.2% (Table 2) it is observed that As (n.d. – 0.071 wt%) and Bi (n.d. – 0.018 wt%) are the elements that show more dispersed content, Ag contents are in the range 0.172–0.198 wt%, Sn in the range 0.105–0.196 wt%, lead in the range 0.278–0.337 wt% and Fe in the range 0.057–0.071 wt%. If this range of compositions is considered to be close to the alloy of the coin, it can a priori be proposed that this coins shows a considerably different pattern of minor elements than the Real Preto coin analysed previously; it is made of almost pure copper with the following average composition (in wt%): 99.23 ± 0.03 copper, 0.027 ± 0.038 arsenic, 0.176 ± 0.019 silver, 0.136 ± 0.052 tin, 0.315 ± 0.032 lead, 0.062 ± 0.008 iron, 0.041 ± 0.037 antimony, and 0.008 ± 0.009 bismuth.

**Table 2**  
2 Reais: Elemental contents (wt%) obtained by XRF. See text for details.

#	Cu	As	Ag	Sn	Pb	Fe	Ti	Cr	Mn	Co	Zn	Sb	Bi
Obverse side													
1	98.42	0.139	0.183	0.159	0.961	0.111	n.d.	n.d.	n.d.	n.d.	n.d.	n.d.	0.024
2	99.28	0.024	0.159	0.143	0.174	0.216	n.d.	n.d.	n.d.	n.d.	n.d.	n.d.	n.d.
3	99.22	0.011	0.162	0.196	0.278	0.057	n.d.	n.d.	n.d.	n.d.	n.d.	0.07	n.d.
4	98.89	n.d.	0.167	0.276	0.529	0.114	n.d.	n.d.	n.d.	0.02	n.d.	n.d.	n.d.
5	98.89	n.d.	0.167	0.247	0.476	0.205	n.d.	n.d.	n.d.	n.d.	0.01	n.d.	0.001
6	94.30	0.041	0.160	0.185	0.332	4.844	n.d.	n.d.	n.d.	n.d.	n.d.	0.09	n.d.
7	93.64	0.065	0.157	0.151	0.354	5.495	n.d.	n.d.	n.d.	n.d.	n.d.	0.09	n.d.
8	84.69	0.117	0.174	0.136	0.437	14.251	n.d.	n.d.	0.11	n.d.	n.d.	0.08	n.d.
9	98.67	0.051	0.166	0.172	0.299	0.559	n.d.	n.d.	n.d.	n.d.	n.d.	0.08	n.d.
10	91.87	0	0.189	0.117	0.350	7.315	n.d.	0.02	0.05	n.d.	n.d.	0.08	0.012
Reverse side													
1	99.48	n.d.	0.139	0.058	0.185	0.104	0.04	n.d.	n.d.	n.d.	n.d.	n.d.	n.d.
2	98.99	0.073	0.163	0.133	0.329	0.234	n.d.	n.d.	n.d.	n.d.	n.d.	0.07	0.007
3	99.42	0.018	0.152	0.071	0.228	0.114	n.d.	n.d.	n.d.	n.d.	n.d.	n.d.	n.d.
4	99.26	n.d.	0.169	0.108	0.330	0.071	n.d.	n.d.	n.d.	n.d.	n.d.	0.05	0.007
5	99.21	0.071	0.198	0.105	0.337	0.057	n.d.	n.d.	n.d.	n.d.	n.d.	n.d.	0.018
6	92.79	n.d.	0.197	0.106	0.394	6.418	n.d.	n.d.	n.d.	n.d.	0.009	0.08	n.d.
7	98.29	n.d.	0.208	0.120	0.400	0.963	n.d.	n.d.	n.d.	n.d.	0.01	n.d.	0.010

n.d. = not detected.

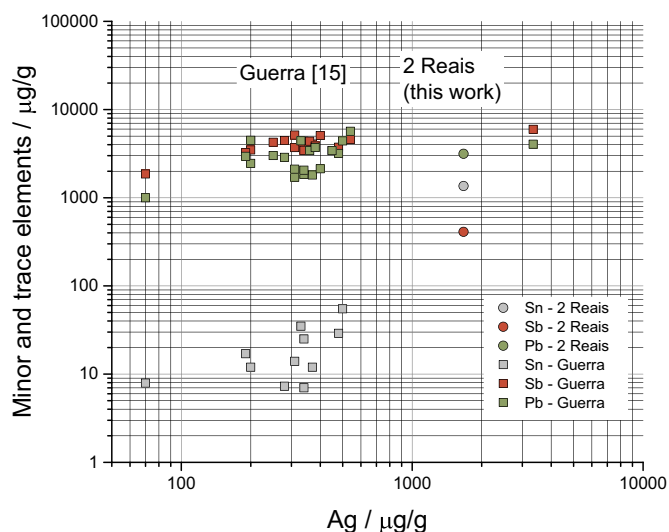


Fig. 9. Evolution of the Sn, Sb, Pb vs Ag composition (in µg/g) of copper coins minted in Portugal in the reign of D. Sebastião [15], and comparison with the 2 Reais results.

If the obtained results are compared with coins minted in the reign of D. Sebastião [15], and thus in the same period (Figs. 6 and 9) it is observed that regarding As, Sn, Sb, Pb and Ag composition the present coin appears to show higher amounts of Ag and Sn, lower amounts of Sb and As and comparable/similar amounts of Pb. Excluding Pb, these results show opposite tendencies than those found in the comparison of the Real Preto coin with its coeval coins (Fig. 7). This indicates that either corrosion, even if present in very small thicknesses, can impact diverse effects in the analytical results or that the present coin shows compositional differences in comparison with other coins from their time. In the case of the 2 Reais, this inconsistency may be explained by history. D. António's reign was very short and unstable because the crown of Spain claimed the Portuguese throne, and invaded Portugal to fight D. António's troops. Given this circumstance it is possible that without the capacity to buy new copper, the Portuguese king may have recycled copper from different origins to mint new coins.

### 3.2. PIXE-EBS results

#### 3.2.1. Real Preto

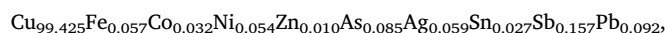
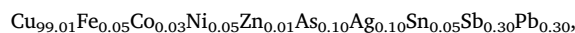
A  $2640 \times 2640 \mu\text{m}^2$  surface PIXE mapping performed on the central part of the obverse side of the coin (inside the area studied by µ-XRF) shows the presence of S, Cl, K, Fe, Co, Ni, Zn, As, Ag, Sb and Pb. As already observed from XRF data, some elements are not homogeneously distributed. Fig. 10 shows the X-ray  $K_{\alpha}$  lines distribution maps (relative

yields) for Cu (8.04 keV) and Ni (7.48 keV).

µ-PIXE and µ-EBS spectra were taken simultaneously at four consecutive points ( $3 \times 4 \mu\text{m}^2$ ) identified in Fig. 10 as RUNS 041, 042, 043 and 044. Two of these points were measured at Ni rich regions (RUNS 041 and 042) and the other two at Ni poor regions (RUNS 043 and 044). Fig. 11 shows the four µ-PIXE spectra and fitted peaks. Table 3 gives the elemental composition obtained from these fits. This table includes the alloy composition proposed from the XRF analysis.

Regarding the PIXE results, it is observed that in the areas with higher contents of P, S, K and Ca, which are elements that are related to dirt deposition and corrosion, there are also higher contents of Fe, Cu, and Pb, and smaller contents in Ni, As and Sb. The negative correlation of Cu with Ni, As and Sb had previously also been detected in the µ-XRF analysis. Here, however, a relation among higher Cu contents and higher contents of (external) elements related to dirt is also suggested. Since Cu and Ni form a solid solution, the heterogeneities observed in the PIXE mapping must be a result of chemical surface alteration, such as corrosion or some type of material deposition.

Even though XRF and PIXE probe different depths thus implying different contributions from the corroded/alterated surface layer, these two techniques present comparable results. The alloy composition for the Real Preto coin (in units of wt% and in units of at.%, respectively) was then set as:



which reflects the composition obtained by XRF with the exception of Fe and Ni concentration values which were lowered: for Fe, an average PIXE value was considered due to the high uncertainty (100%) of XRF value; for Ni, we considered the lowest values obtained by PIXE, which is one third of the XRF value. The difference that resulted from these modifications was removed by renormalization.

With this composition, the degrees of freedom for the trace elements depth distribution are effectively restricted when performing EBS spectra fitting. The same method was applied to the four points analysed. The full elemental depth profile information is on Tables 4 to 7 and the depth profile plots are on Figs. 12-15. Figs. 12 and 13 relate to the analysis with higher Ni contents (RUNS 041 and 042). Figs. 14 and 15 relate to the analysis with poorer Ni contents (RUNS 043 and 044). It is visible the relevance of performing a self-consistent analysis using the PIXE data to fit the EBS spectrum: the copper signal dominates the signals from all other elements that even more are overlapping (exception for C and O). The level of agreement between PIXE data and the EBS fit is inferred from the bar graph at bottom right. Here, the red bar gives the peak area obtained by GUPIXWIN when fitted the PIXE spectrum and the blue bar gives the X-ray yield calculated by Data-Furnace for the given matrix environment. When the two bars coincide,

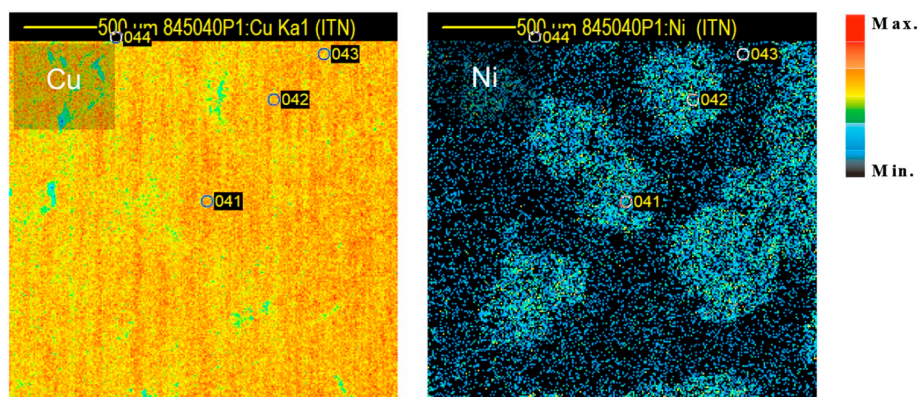


Fig. 10. Real Preto (D. Duarte): PIXE elemental surface maps for Cu  $K_{\alpha}$ , and Ni  $K_{\alpha}$ , obtained with a 2 MeV proton beam ( $2640 \times 2640 \mu\text{m}^2$ ).

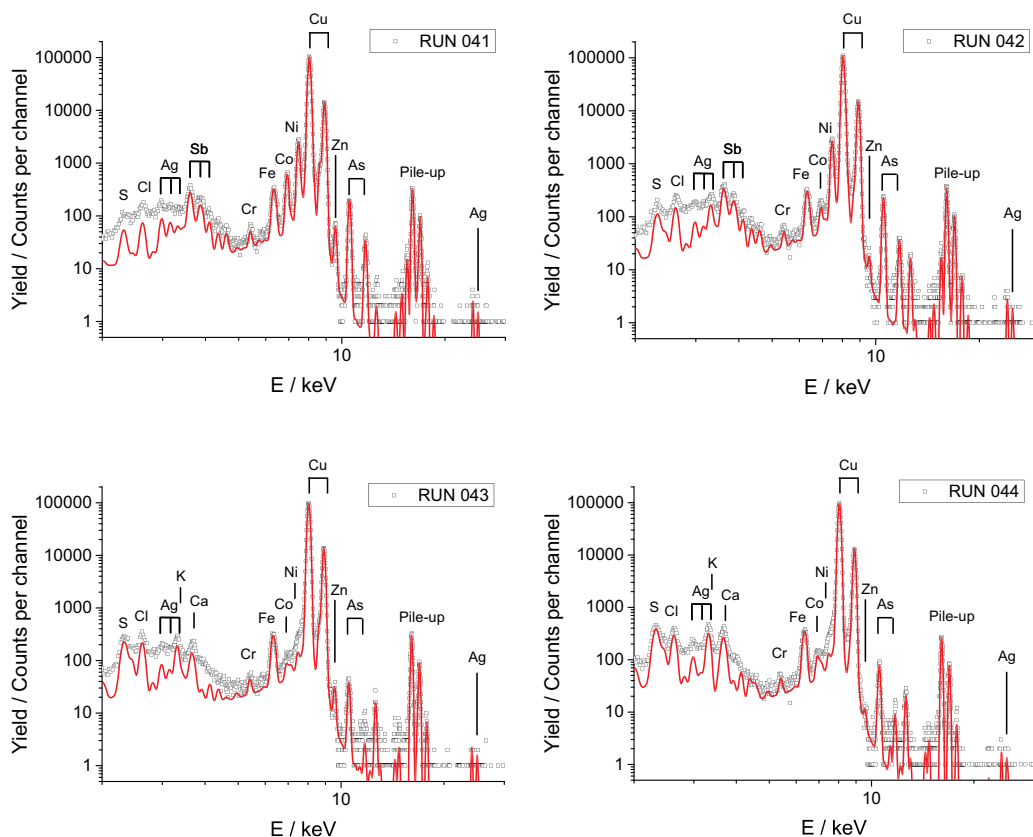


Fig. 11. Real Preto (D. Duarte): PIXE spectra (points) and fitted peaks (line).

Table 3

Real Preto: Elemental contents (wt%) obtained by PIXE and XRF (partial). See text for details.

Z		PIXE				XRF
		RUN 041	RUN 042	RUN 043	RUN 044	
15	P	0.023 ± 0.025	0.06 ± 0.03	0.13 ± 0.03	0.28 ± 0.05	n.d.
16	S	0.06 ± 0.02	0.10 ± 0.02	0.24 ± 0.02	0.44 ± 0.03	n.d.
17	Cl	0.047 ± 0.007	0.098 ± 0.008	0.17 ± 0.01	0.23 ± 0.02	n.d.
19	K	0.012 ± 0.004	0.048 ± 0.006	0.07 ± 0.01	0.131 ± 0.006	n.d.
20	Ca	n.d.	n.d.	0.036 ± 0.007	0.096 ± 0.010	n.d.
22	Ti	n.d.	0.002 ± 0.001	n.d.	0.003 ± 0.001	n.d.
24	Cr	0.008 ± 0.002	0.007 ± 0.001	0.007 ± 0.001	0.007 ± 0.001	n.d.
26	Fe	0.056 ± 0.004	0.036 ± 0.003	0.055 ± 0.004	0.090 ± 0.004	0.12 ± 0.12
27	Co	0.214 ± 0.005	0.035 ± 0.003	0.016 ± 0.003	0.030 ± 0.003	0.031 ± 0.009
28	Ni	1.59 ± 0.02	1.63 ± 0.02	0.046 ± 0.007	0.040 ± 0.008	0.13 ± 0.02
29	Cu	95.4 ± 0.2	95.9 ± 0.2	98.0 ± 0.2	97.3 ± 0.2	98.8 ± 0.2
30	Zn	1.06 ± 0.05	0.21 ± 0.05	0.51 ± 0.05	0.12 ± 0.05	0.010
33	As	1.10 ± 0.03	1.06 ± 0.03	0.08 ± 0.02	0.27 ± 0.03	0.127 ± 0.008
47	Ag	0.10 ± 0.02	0.08 ± 0.01	0.12 ± 0.02	0.17 ± 0.02	0.107 ± 0.002
50	Sn	0.04 ± 0.01	0.04 ± 0.02	0.04 ± 0.02	0.05 ± 0.02	0.061 ± 0.007
51	Sb	0.26 ± 0.02	0.24 ± 0.02	n.d.	0.10 ± 0.03	0.29 ± 0.02
82	Pb	n.d.	0.43 ± 0.11	0.47 ± 0.05	0.63 ± 0.07	0.33 ± 0.03

n.d. = not detected.

Table 4

Real Preto: elemental depth profiles (at.%) – Run 041.

10 <sup>15</sup> at/cm <sup>2</sup>	nm	Cu+	C	O	S	Cl	K	Cr	Fe	Co	Ni	Zn	As	Ag	Sn	Sb
5800	719	65.7	4.5	8.9	0.12	0.11	0.04	0.04	0.17	1.89	10.03	5.90	2.45	0.045	0.017	0.100
4100	492	79.7	4.5	3.4	0.12	0.06	0.03	0.03	0.11	0.68	5.65	3.28	2.26	0.034	0.011	0.091
Bulk		100	0	0	0	0	0	0	0	0	0	0	0	0	0	0

Cu + stands for Cu<sub>99.425</sub>Fe<sub>0.057</sub>Co<sub>0.032</sub>Ni<sub>0.054</sub>Zn<sub>0.010</sub>As<sub>0.085</sub>Ag<sub>0.059</sub>Sn<sub>0.027</sub>Sb<sub>0.157</sub>Pb<sub>0.092</sub>.

**Table 5**  
Real Preto: Elemental depth profiles (at.%) – Run 042.

$10^{15}$ at/cm <sup>2</sup>	nm	Cu+	C	O	S	Cl	K	Cr	Fe	Co	Ni	Zn	As	Ag	Sn	Sb	Pb
1500	200	15.2	3.0	25.4	0.601	0.62	0.578	0.175	0.024	0.594	46.8	0.35	6.16	0.058	0.06	0.34	0.07
1220	365	27.6	21.9	30.3	0.035	0.15	0.051	0.039	0.008	0.137	4.8	6.54	8.39	0.038	0	0	0.03
Bulk		100	0	0	0	0	0	0	0	0	0	0	0	0	0	0	0

Cu + stands for  $Cu_{99.425}Fe_{0.057}Co_{0.032}Ni_{0.054}Zn_{0.010}As_{0.085}Ag_{0.059}Sn_{0.027}Sb_{0.157}Pb_{0.092}$ .

**Table 6**  
Real Preto: Elemental depth profiles (at.%) – Run 043.

$10^{15}$ at/cm <sup>2</sup>	nm	Cu+	C	O	S	Cl	K	Cr	Fe	Ni	Zn	As	Ag	Sn	Pb	P	Ca
1715	210	36.03	32.15	24.52	0.52	0.63	0.55	0.124	0.152	0.07	4.58	0	0.156	0.0059	0.13	0.26	0.14
4015	530	72.09	3.47	22.55	0.34	0.13	0.04	0.011	0.090	0	0.94	0	0.005	0.0062	0.13	0.13	0.07
4225	525	75.65	8.95	13.93	0.22	0.13	0.04	0.008	0.067	0	0.69	0	0.001	0.0004	0.13	0.14	0.06
7560	940	76.86	7.27	13.84	0.16	0.15	0.05	0.003	0.066	0	1.29	0	0	0	0.13	0.11	0.08
Bulk		100	0	0	0	0	0	0	0	0	0	0	0	0	0	0	0

Cu + stands for  $Cu_{99.425}Fe_{0.057}Co_{0.032}Ni_{0.054}Zn_{0.010}As_{0.085}Ag_{0.059}Sn_{0.027}Sb_{0.157}Pb_{0.092}$ .

**Table 7**  
Real Preto: Elemental depth profiles (at. %) – Run 044.

$10^{15}$ at/cm <sup>2</sup>	nm	Cu+	C	O	S	Cl	K	Cr	Fe	Ni	Zn	As	Ag	Sn	Pb	P	Ca
24,900	295	41.7	30.1	24.6	0.71	0.37	0.33	0.04	0.37	0.052	0.44	0.31	0.08	0.021	0.26	0.35	0.24
4415	570	67.3	8.4	21.3	0.60	0.32	0.22	0.03	0.32	0.052	0.42	0.31	0.06	0.010	0.21	0.34	0.17
4150	545	72.0	5.7	20.2	0.43	0.26	0.14	0.02	0.10	0.020	0.29	0.20	0.04	0	0.16	0.34	0.16
7500	940	79.0	5.4	14.1	0.27	0.26	0.16	0	0.05	0	0.10	0.10	0.02	0	0.16	0.25	0.19
Bulk		100	0	0	0	0	0	0	0	0	0	0	0	0	0	0	0

Cu + stands for  $Cu_{99.425}Fe_{0.057}Co_{0.032}Ni_{0.054}Zn_{0.010}As_{0.085}Ag_{0.059}Sn_{0.027}Sb_{0.157}Pb_{0.092}$ .

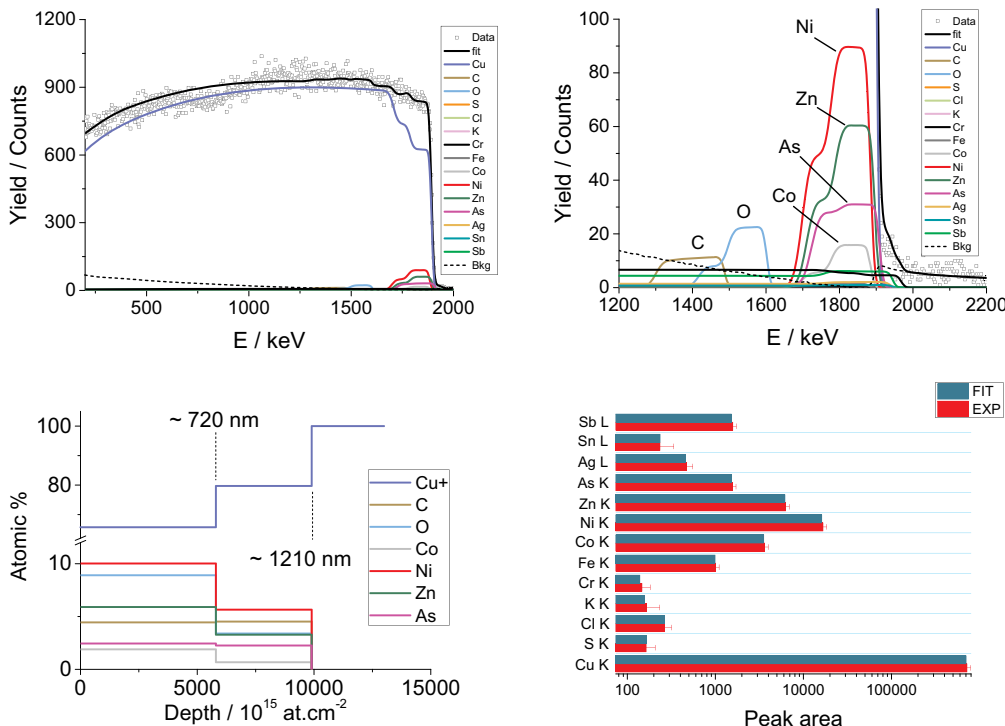


**Fig. 12.** Real Preto (D. Duarte) – RUN 041 (Ni rich). Top left: EBS spectrum fitted with data furnace. Top right: fitted spectrum close-up. Bottom left: Elemental depth profile obtained from the fit to the EBS spectrum. Bottom right: PIXE results (see text for details). Cu+ stands for

$Cu_{99.425}Fe_{0.057}Co_{0.032}Ni_{0.054}Zn_{0.010}As_{0.085}Ag_{0.059}Sn_{0.027}Sb_{0.157}Pb_{0.092}$ .

there is a perfect match between PIXE data and EBS fit. The elemental depth profile, which results from the EBS spectrum fit, is represented by finite layers with constant concentration at bottom left. For the sake of simplicity, only the more abundant elements are represented in the plot. In these plots, depth is represented in  $10^{15}$  atcm<sup>-2</sup>, which are the

“natural” units in EBS. The conversion to nanometre requires the knowledge of the atomic density which, for these complex structures is not known. The values presented in nanometres were computed by the DataFurnace code by assuming that each layer thickness is the weighted average of the elemental densities. This assumption gives reasonable

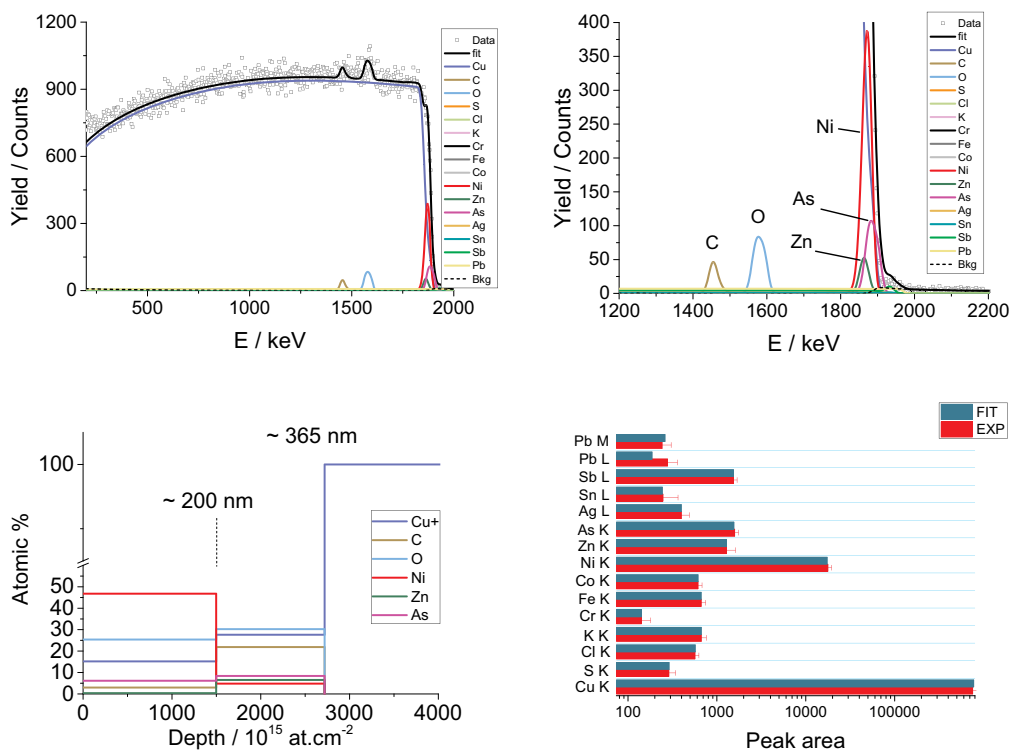


Fig. 13. Real Preto (D. Duarte) – RUN 042 (Ni rich). Top left: EBS spectrum fitted with data furnace. Top right: fitted spectrum close-up. Bottom left: Elemental depth profile obtained from the fit to the EBS spectrum. Bottom right: PIXE results.

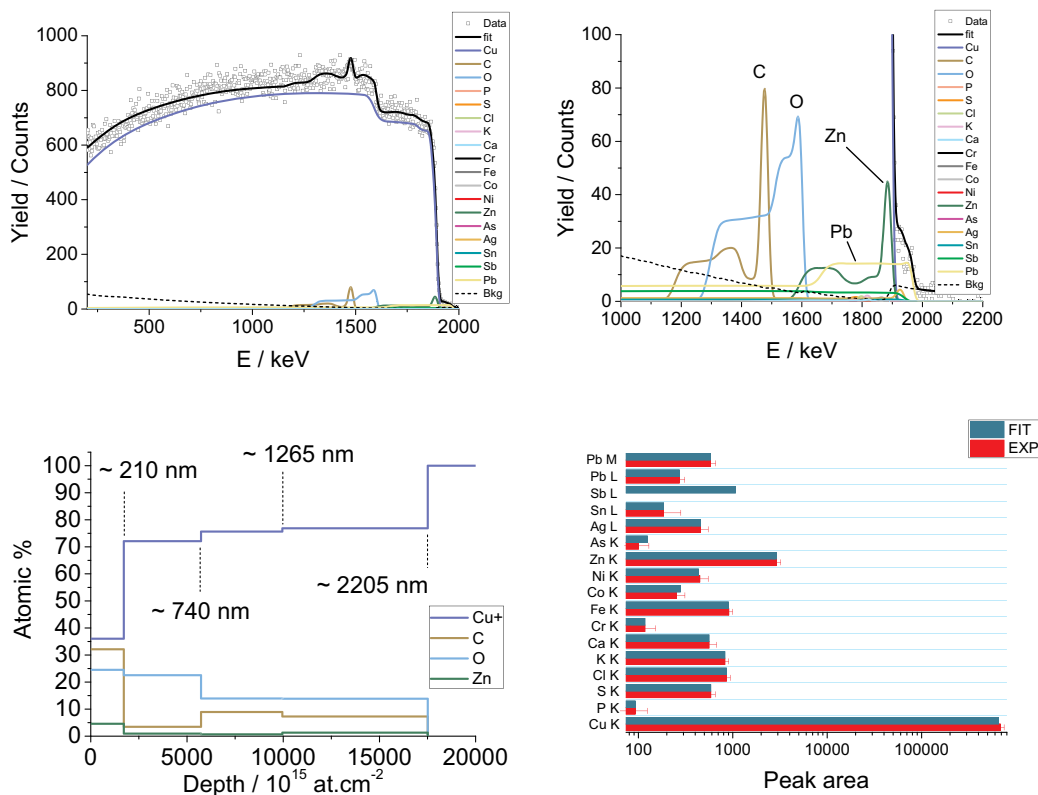


Fig. 14. Real Preto (D. Duarte) – RUN 043 (Ni poor). Top left: EBS spectrum fitted with data furnace. Top right: fitted spectrum close-up. Bottom left: Elemental depth profile obtained from the fit to the EBS spectrum. Bottom right: PIXE results.

estimates as shown in the following comparison between copper and two common copper oxides (cuprite and malachite): Cu (8.92 g·cm<sup>-3</sup>), Cu<sub>2</sub>O (6.1 g·cm<sup>-3</sup>) and Cu<sub>2</sub>(CO<sub>3</sub>)(OH)<sub>2</sub> (4.05 g·cm<sup>-3</sup>) have atomic

densities that change by < 50%: 8.45 × 10<sup>22</sup> at·cm<sup>-3</sup> for Cu; 7.70 × 10<sup>22</sup> at·cm<sup>-3</sup> for Cu<sub>2</sub>O and 11.0 × 10<sup>22</sup> at·cm<sup>-3</sup> for Cu<sub>2</sub>(CO<sub>3</sub>)(OH)<sub>2</sub>.

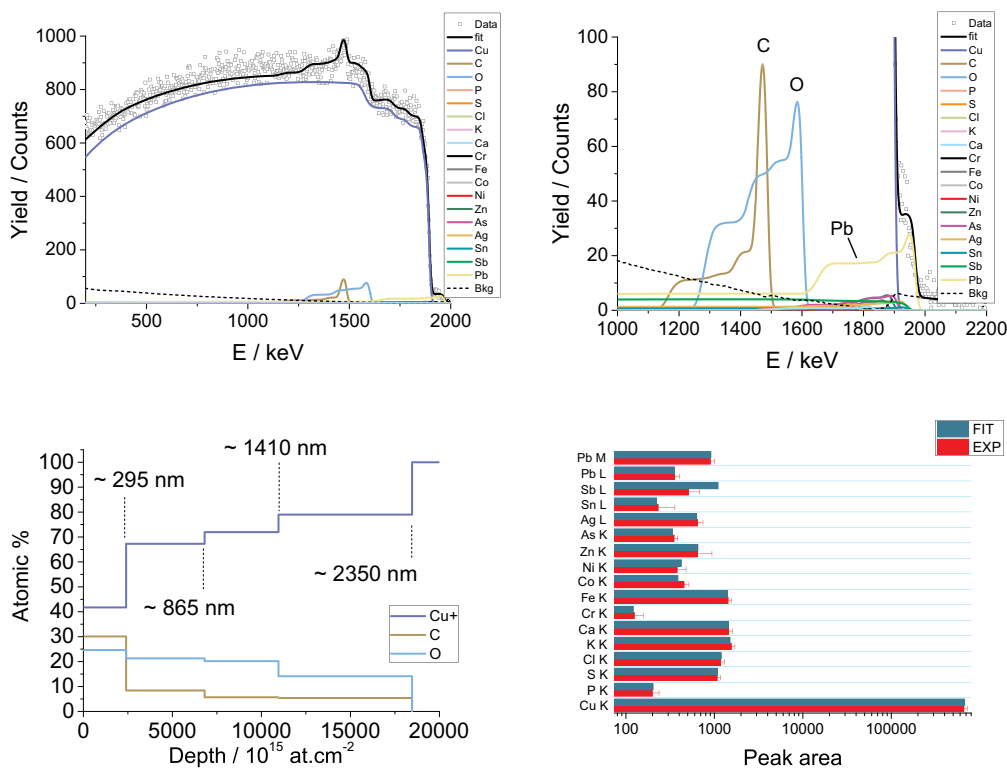


Fig. 15. Real Preto (D. Duarte) – RUN 044(Ni poor). Top left: EBS spectrum fitted with data furnace. Top right: fitted spectrum close-up. Bottom left: Elemental depth profile obtained from the fit to the EBS spectrum. Bottom right: PIXE results.

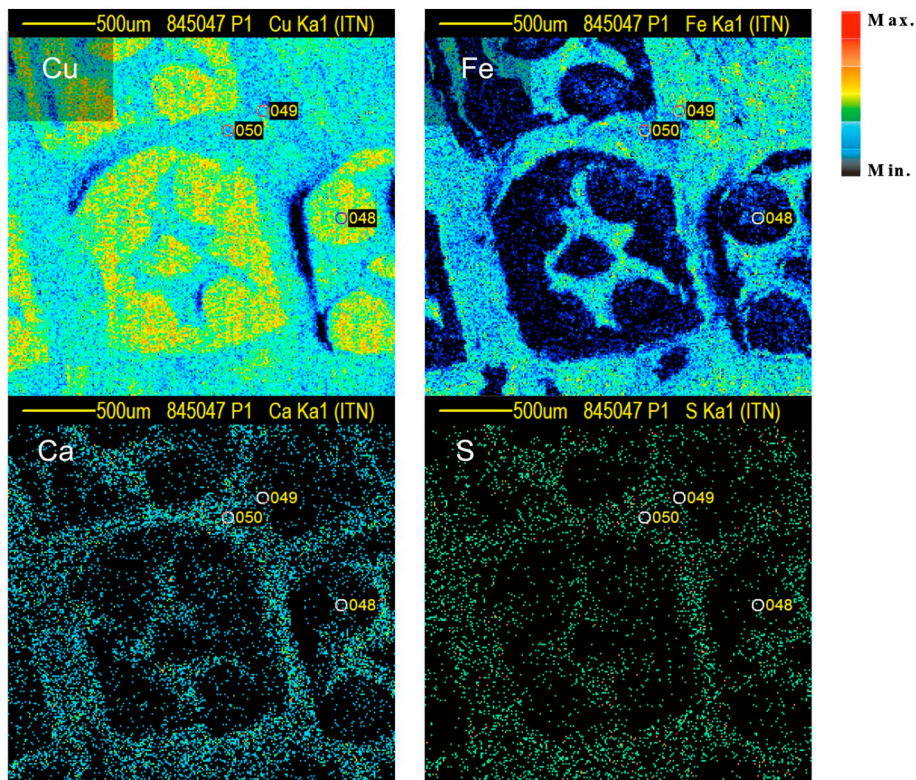


Fig. 16. 2 Reais (D. António): PIXE elemental surface maps for Cu K<sub>α</sub>, Fe K<sub>α</sub>, Ca K<sub>α</sub> and S K<sub>α</sub>, obtained with a 2 MeV proton beam (2640 × 2640 μm<sup>2</sup>).

The results show depth profiles that reach just over 1200 nm in the Ni rich areas and over 2350 nm in the Ni poor areas. Considering that these profiles represent the corrosion/alteration layer until bulk/unaltered metal, it can be considered that the corrosion/alterated layer is

very thin (just up to 2 μm). Along these profiles copper content is always increasing towards the bulk and other elements, such as C, O, Co, Ni, Zn, As are decreasing. Only in one depth profile from a Ni rich area (Fig. 13, RUN 042) it is observed and intermediate layer with higher C,

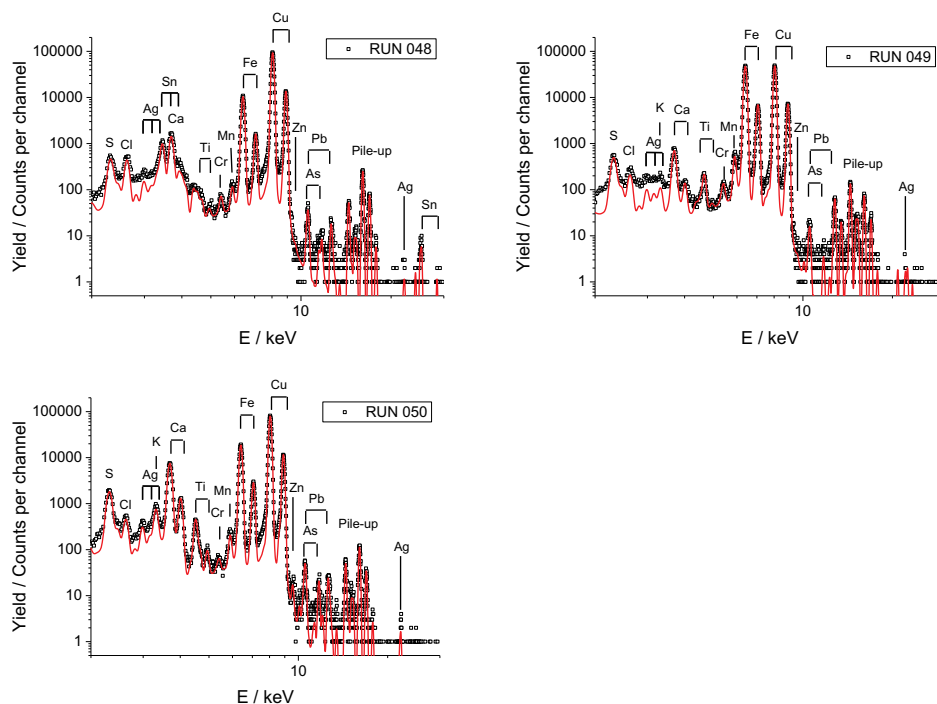


Fig. 17. 2 Reais (D. António): PIXE spectra (points) and fitted peaks (line).

Table 8

2 Reais: Elemental concentrations (wt%) obtained by PIXE and XRF (partial). See text for details.

Z		PIXE			XRF
		RUN 048	RUN 049	RUN 050	
16	S	0.59 ± 0.03	0.82 ± 0.04	2.68 ± 0.05	n.d.
17	Cl	0.323 ± 0.012	0.175 ± 0.013	0.328 ± 0.015	n.d.
19	K	0.056 ± 0.007	0.032 ± 0.005	0.241 ± 0.009	n.d.
20	Ca	0.259 ± 0.012	0.229 ± 0.008	2.30 ± 0.02	n.d.
22	Ti	0.018 ± 0.002	0.010 ± 0.003	0.131 ± 0.004	n.d.
24	Cr	0.013 ± 0.002	0.028 ± 0.003	0.009 ± 0.002	n.d.
25	Mn	0.025 ± 0.002	0.194 ± 0.006	0.058 ± 0.003	n.d.
26	Fe	3.94 ± 0.02	23.67 ± 0.06	7.61 ± 0.03	0.062 ± 0.008
27	Co	0.036 ± 0.010	0.20 ± 0.05	0.05 ± 0.02	n.d.
29	Cu	92.8 ± 0.2	74.3 ± 0.2	85.3 ± 0.2	99.23 ± 0.03
30	Zn	0.02 ± 0.04	0.02 ± 0.04	0.23 ± 0.04	n.d.
33	As	0.044 ± 0.014	0.072 ± 0.015	0.09 ± 0.02	0.027 ± 0.038
47	Ag	0.16 ± 0.02	0.13 ± 0.02	0.36 ± 0.03	0.176 ± 0.019
50	Sn	1.12 ± 0.03	n.d.	0.07 ± 0.03	0.136 ± 0.052
51	Sb	n.d.	n.d.	n.d.	0.041 ± 0.037
82	Pb	0.47 ± 0.05	0.10 ± 0.06	0.56 ± 0.06	0.315 ± 0.032
83	Bi	n.d.	n.d.	n.d.	0.008 ± 0.009

n.d. = not detected.

Table 9

2 Reais: Elemental depth profiles (at.%) – Run 048.

10 <sup>15</sup> at/cm <sup>2</sup>	nm	Cu +	C	O	Fe	S	Cl	Ca	Cr	K	Mn	Ti	Sn	Pb
2900	430	25.74	13.54	47.48	10.49	0.81	0.48	0.62	0.038	0.114	0.076	0.048	0.477	0.095
10,000	1275	61.99	5.68	15.16	13.68	0.89	0.42	0.63	0.032	0.116	0.074	0.053	1.158	0.105
3000	410	57.59	6.15	18.57	14.54	0.78	0.45	0.62	0.034	0.101	0.067	0.045	1.007	0.056
3000	385	73.79	0.00	12.50	10.87	0.71	0.33	0.60	0.033	0.087	0.054	0.033	0.978	0.022
Bulk		100	0	0	0	0	0	0	0	0	0	0	0	0

Cu + stands for Cu<sub>99.554</sub>Fe<sub>0.070</sub>As<sub>0.040</sub>Ag<sub>0.156</sub>Sn<sub>0.073</sub>Pb<sub>0.107</sub>.

O, Zn and As, which can represent a local discontinuity in the corrosion composition, i.e. the formation of an intermediate corrosion layer with accumulation of these elements.

The depth profiles show that the superficial higher contents of As,

Ni and Zn are always accompanied by the presence of O and C. This demonstrates that the corrosion layer will tend to show higher contents in these elements and less content of copper, when compared to bulk composition. For RUNS 041 and 042 (Ni rich regions), PIXE data gives

**Table 10**  
2 Reais: Elemental depth profiles (at.%) – Run 049.

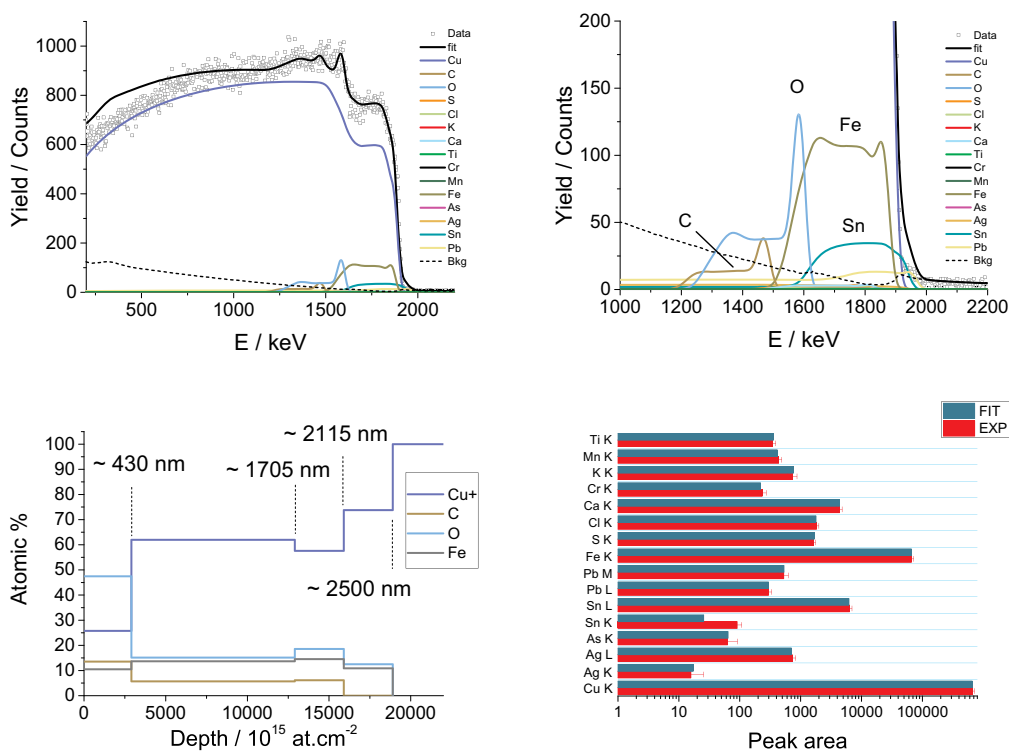
$10^{15}$ at/cm <sup>2</sup>	nm	Cu +	C	O	Fe	S	Cl	Ca	Cr	K	Mn	Ti
2900	445	47.35	3.16	43.29	0.81	2.16	0.59	1.95	0.05	0.04	0.59	0.02
1000	145	8.56	16.09	44.80	25.38	2.66	0.30	1.51	0.05	0.04	0.60	0.02
8000	1175	10.53	10.53	47.07	31.27	0	0	0	0.04	0.04	0.50	0.02
8000	1025	24.95	1.67	16.79	56.29	0	0	0	0.04	0.03	0.20	0.02
5000	590	42.84	0	0	56.97	0	0	0	0	0	0.1	0
3000	355	55.24	0	0	44.64	0	0	0	0.04	0.03	0.05	0
5000	590	64.93	0	0	35.03	0	0	0	0.04	0	0	0
3000	355	69.23	0	0	30.77	0	0	0	0	0	0	0
Bulk		100	0	0	0	0	0	0	0	0	0	0

Cu + stands for  $Cu_{99.554}Fe_{0.070}As_{0.040}Ag_{0.156}Sn_{0.073}Pb_{0.107}$ .

**Table 11**  
2 Reais: Elemental depth profiles (at.%) – Run 050.

$10^{15}$ at/cm <sup>2</sup>	nm	Cu +	C	O	Fe	S	Cl	Ca	Cr	K	Mn	Ti	Sn	Pb	As	Ag	Sn
695	80	59.05	29.84	6.38	0.00	0.01	0.006	0.002	0.016	2.279	0.700	1.14	0.005	0	0.08	0.07	0.42
7890	820	3.36	71.06	17.55	4.20	0.45	0.015	2.566	0.010	0.126	0.065	0.08	0.010	0	0.03	0.06	0.42
5510	575	12.02	65.80	12.53	4.74	1.90	0.174	1.999	0.015	0.192	0.072	0.10	0.008	0.01	0.03	0.07	0.35
8000	1045	31.74	24.26	24.26	9.72	5.14	0.674	3.073	0.020	0.274	0.088	0.26	0.008	0.10	0.04	0.07	0.27
9100	1210	25.67	10.57	21.75	36.03	0.0	0	5.025	0.0	0.148	0.085	0.14	0.005	0.24	0.03	0.13	0.16
Bulk		100	0	0	0	0	0	0	0	0	0	0	0	0	0	0	0

Cu + stands for  $Cu_{99.554}Fe_{0.070}As_{0.040}Ag_{0.156}Sn_{0.073}Pb_{0.107}$ .



**Figs. 18, 2.** Reais (D. António) – RUN 048 (Fe poor). Top left: EBS spectrum fitted with data furnace. Top right: fitted spectrum close-up. Bottom left: Elemental depth profile obtained from the fit to the EBS spectrum. Bottom right: PIXE results.

identical Ni contents,  $1.59 \pm 0.02$  and  $1.63 \pm 0.02$  (Table 3), respectively. The corresponding EBS spectra show that this content similarity does not correspond to similar depth distributions, though. In RUN 041, the highest Ni concentration is 10 at.% and extends up to ~1210 nm, while in RUN 042, the highest Ni concentration is considerably higher (46.8 at.%) but extends only up to ~365 nm.

3.2.2. 2 Reais

A  $2640 \times 2640 \mu\text{m}^2$  surface PIXE mapping performed on the central

part of the obverse side of the coin (inside the area covered by  $\mu$ -XRF) shows the presence of S, Cl, K, Fe, Co, Ni, Zn, As, Ag, Sb and Pb. As already observed from XRF data, elements are not homogeneously distributed. Fig. 16 shows the X-ray surface elemental distribution maps (relative yield) for the  $K_{\alpha}$  line of Cu (8.04 keV), Fe (6.40 keV), Ca (3.69 keV) and S (2.31 keV).

$\mu$ -PIXE and  $\mu$ -EBS spectra were taken simultaneously at three consecutive points ( $3 \times 4 \mu\text{m}^2$ ) identified in Fig. 16 as RUNS 048, 049 and 050. Two of these points were measured at Fe rich regions (RUNS 049

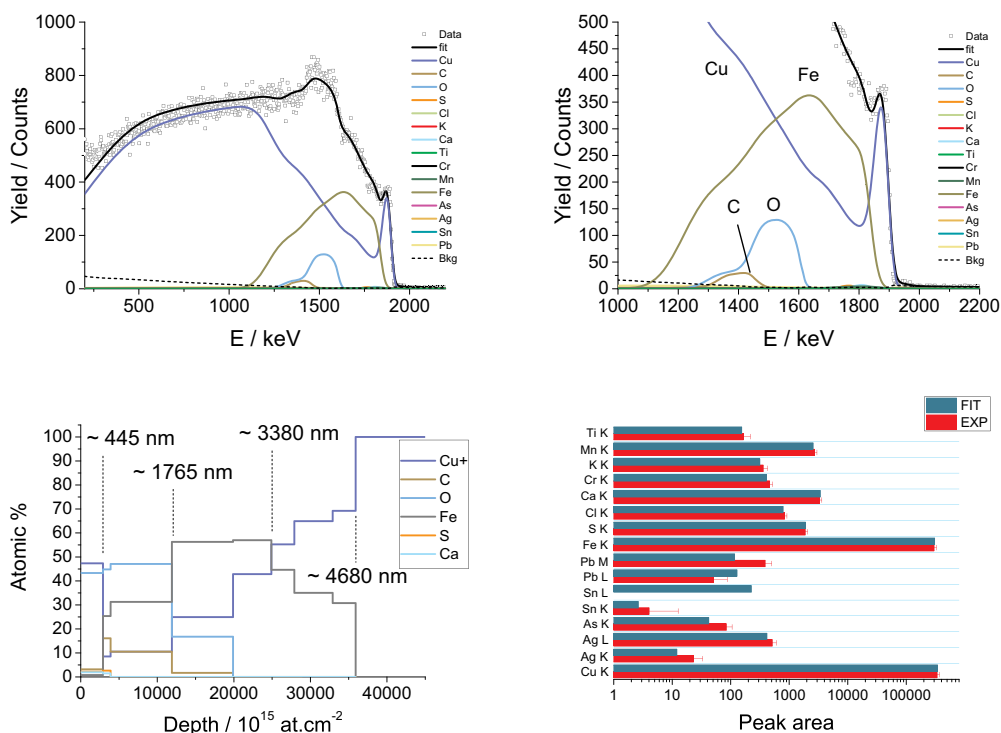


Fig. 19. 2 Reais (D. António) – RUN 049 (Fe rich). Top left: EBS spectrum fitted with data furnace. Top right: fitted spectrum close-up. Bottom left: Elemental depth profile obtained from the fit to the EBS spectrum. Bottom right: PIXE results.

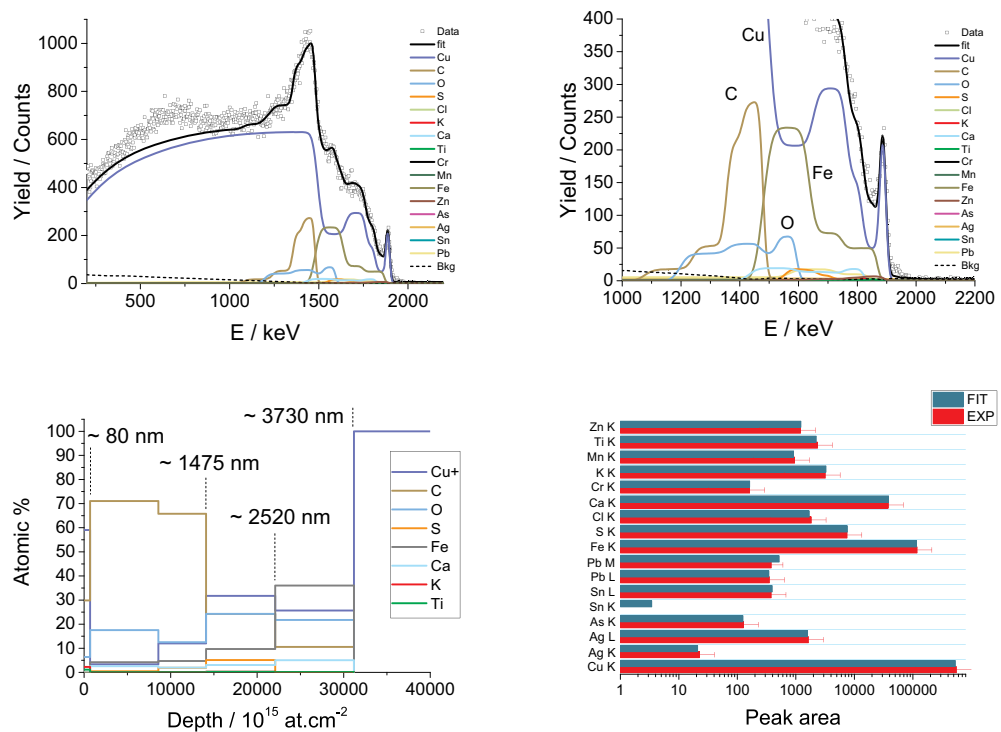
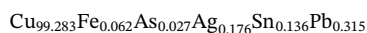


Fig. 20. 2 Reais (D. António) – RUN 050 (Fe rich). Top left: EBS spectrum fitted with data furnace. Top right: fitted spectrum close-up. Bottom left: Elemental depth profile obtained from the fit to the EBS spectrum. Bottom right: PIXE results.

and 050) and the third one at a Fe poor region (RUN 048). Fig. 17 shows the three  $\mu$ -PIXE fitted spectra and Table 8 gives the elemental composition obtained from these fits. This table includes the alloy composition proposed from the XRF analysis.

PIXE results show for all three points a considerable presence of Fe, S, Cl, K, Ca, Ti, Cr and Mn which are elements that are related to dirt

deposition and corrosion. This prevents a direct comparison with  $\mu$ -XRF analysis, so we define a bulk composition for the 2 Reais as an almost pure copper with the following average composition (in units of wt% and in units of at.%, respectively):





which reflects the composition proposed from the XRF analysis but renormalized by removal of Sb and Bi: both elements present very high uncertainties and were not detected by PIXE.

Identically to the previously analysed coin, the degrees of freedom for the trace elements depth distribution are effectively restricted when performing EBS spectra fitting. The full elemental depth profile information is on Tables 9-11 and the depth profile plots are on Figs. 18-20. Fig. 18 refers to the analysis with lower Fe content (RUN 048). Figs. 19 and 20 relate to the point analyses with richer Fe contents (RUNS 049 and 050). Also, in these points, the level of agreement between PIXE data and the EBS fit is very good.

In the present coin the depths of alteration/corrosion are thicker (up to 4.7  $\mu\text{m}$ ) than in the previous coin, and it is possible to identify some sub-layers based on differences on element concentrations. In two analysed spots it is possible to observe a very thin copper-enriched sub-layer which is present as an intermediate layer of corrosion (Figs. 19 and 20). This sub-layer may represent an accumulation of leached copper, and its presence may indicate that this coin was probably subjected to less surface cleaning actions (e.g. mechanical cleaning that could remove the most superficial thin sub-layers). High Fe contents (up to 40 at.%) are distributed to depths close to the bulk and in all cases internal layers of alteration can show higher contents than the most superficial layers. In two analysed spots oxygen (exogenous element) follows the presence of iron along the profile, indicating that these sub-layers are altered/corroded regions. Only in one of the analyses (Fig. 19) the presence of high contents of Fe (~40 at.%) in an inner sub-layer without O and C was detected. The presence of such sub-layer can be explained by the presence of an iron-rich inclusion in the copper metal matrix, due to the low solubility of iron in copper.

#### 4. Conclusions

The altered surfaces of two centennial Portuguese copper coins were successfully characterized using a combination of XRF, PIXE and EBS. An estimate of elemental depth distribution in corrosion/alteration profiles resulted from the fits to EBS spectra in a self-consistent analysis with PIXE spectra taken simultaneously. XRF data with contribution from PIXE was used to define the coins near bulk composition. EBS depth profile was able to determine the depth of corrosion (of up to ~2.3  $\mu\text{m}$  for coin Real Preto and up to ~4.7  $\mu\text{m}$  for coin 2 Reais), and distinguish sub-layers based on the elements' distribution profiles. It was found a superficial sub-layer Ni-rich (up to 40 at.% Ni and of 0.2–0.7  $\mu\text{m}$ ) in Real Preto coin and a sub-layer Fe-rich (up to 50 at.% and of ~1  $\mu\text{m}$ ) in 2 Reais coin (which in one spot analysis can be explained as presence of a local Fe metallic particle). The estimated near-bulk composition determined for the coins shows some discrepancies with compositions determined in past works for Sn, Pb, Bi and Ag in coeval coins, especially in terms of silver content. The distribution of this element (Ag) along the alteration/corrosion profile was not possible to evaluate (due to its very low content) and the presence of Ni and Fe very rich sub-layers in the coins can raise some concerns regarding surface or conservation treatments in the past. Thus, the elemental information gathered in the present study can raise some doubts about the coins' authenticities.

#### Declaration of competing interest

The authors declare that they have no known competing financial interests or personal relationships that could have appeared to influence the work reported in this paper.

#### Acknowledgments

J. Cruz acknowledges LIBPhys (UID/FIS/04559/2019) and NOVA.ID.FCT. V. Corregidor and L.C. Alves acknowledge support from UID/Multi/04349/2019 project. E. Figueiredo and R. J. C. Silva acknowledge FCT and COMPETE2020 funding for the project (UID/CTM/50025/2019). We gratefully acknowledge the most helpful discussions with R. Borges.

#### Data availability

The raw/processed data required to reproduce these findings cannot be shared at this time as the data also forms part of an ongoing study.

#### References

- [1] B. Liss, S. Stout, Materials characterization for cultural heritage: XRF case studies in archaeology and art, in: M. Vincent, V. López-Menchero Bendicho, M. Ioannides, T. Levy (Eds.), *Heritage and Archaeology in the Digital Age. Quantitative Methods in the Humanities and Social Sciences*, Springer, Cham, 2017, [https://doi.org/10.1007/978-3-319-65370-9\\_3](https://doi.org/10.1007/978-3-319-65370-9_3).
- [2] G. Gigante et al. Identification Techniques II. In: Varella E. (ed) *Conservation Science for the Cultural Heritage: Applications of Instrumental Analysis*. Springer. (2013). Doi:<https://doi.org/10.1007/978-3-642-30985-4>.
- [3] E. Figueiredo, R.J.C. Silva, F.M.B. Fernandes, M.F. Araújo, Some long term corrosion patterns in archaeological metal artefacts, *Mater. Sci. Forum* 636–637 (2010) 1030–1035.
- [4] S. Pessanha, M. Costa, M. Oliveira, M. Jorge, M.L. Carvalho, Nondestructive analysis of Portuguese “dinheiros” using XRF: overcoming patina constraints, *Appl. Phys. A Mater. Sci. Process.* 119 (2015) 1173–1178, <https://doi.org/10.1007/s00339-015-9087-2>.
- [5] V. Corregidor, A.R. Oliveira, P.A. Rodrigues, L.C. Alves, Paintings on copper by the Flemish artist Frans Francken II: PIXE characterization by external microbeam, *Nucl. Instr. and Meth. in Phys. Res. B* 348 (2015) 291–295, <https://doi.org/10.1016/j.nimb.2014.12.072>.
- [6] L. Beck, E. Alloin, C. Berthier, S. Réveillon, V. Costa, Silver surface enrichment controlled by simultaneous RBS for reliable PIXE analysis of ancient coins, *Nucl. Instr. and Meth. in Phys. Res. B* 266 (2008) 2320–2324, <https://doi.org/10.1016/j.nimb.2008.03.084>.
- [7] I. Llorente, M. Castellote, R. Gonzalez-Arrabal, M.D. Ynsa, A. Muñoz-Martin, P.G. de Viedma, A. Castillo, I. Martínez, C. Andrade, P. Zuloaga, M. Ordoñez, PIXE/RBS as a tool to study cementitious materials: application to the dynamic leaching of concrete, *Nucl. Instr. and Meth. in Phys. Res. B* 267 (2009) 3670–3674, <https://doi.org/10.1016/j.nimb.2009.09.028>.
- [8] L. Beck, C. Jeynes, N.P. Barradas, Characterization of paint layers by simultaneous self-consistent fitting of RBS/PIXE spectra using simulated annealing, *Nucl. Instr. and Meth. in Phys. Res. B* 266 (2008) 1871–1874, <https://doi.org/10.1016/j.nimb.2007.12.091>.
- [9] V. Corregidor, L.C. Alves, N.P. Barradas, M.A. Reis, M.T. Marques, J.A. Ribeiro, Characterization of mercury gilding art objects by external proton beam, *Nucl. Instr. and Meth. in Phys. Res. B* 269 (24) (2011) 3049–3053, <https://doi.org/10.1016/j.nimb.2011.04.070>.
- [10] J. Cruz, V. Corregidor, L. Alves, Simultaneous use and self-consistent analyses of  $\mu$ -PIXE and  $\mu$ -EBS for the characterization of corrosion layers grown on ancient coins, *Nucl. Instr. and Meth. in Phys. Res. B* 406 (2017) 324–328, <https://doi.org/10.1016/j.nimb.2017.02.010>.
- [11] C. Jeynes, M.J. Bailey, N.J. Bright, M.E. Christopher, G.W. Grime, B.N. Jones, V.V. Palitsin, R.P. Webb, “Total IBA” – Where are we? *Nucl. Instr. and Meth. in Phys. Res. B* 271 (2012) 107–118, <https://doi.org/10.1016/j.nimb.2011.09.020>.
- [12] N.P. Barradas, C. Jeynes, Advanced physics and algorithms in the IBA DataFurnace, *Nucl. Instr. and Meth. in Phys. Res. B* 266 (2008) 1875–1879, <https://doi.org/10.1016/j.nimb.2007.10.044>.
- [13] E. Pernicka, Trace element fingerprinting of ancient copper: A guide to technology or provenance? in: M.M. Young, A.M. Pollard, P. Budd, R.A. Ixer (Eds.), *Metals in Antiquity, BAR International Series*, 792 1999, pp. 163–171.
- [14] E. Pernicka, Archaeometallurgy in global perspective. methods and syntheses, Chapter: Provenance Determination of Archaeological Metal Objects, Publisher: Springer Editors: B.W. Roberts, C. Thornton (2014), 239–268. Doi:[https://doi.org/10.1007/978-1-4614-9017-3\\_11](https://doi.org/10.1007/978-1-4614-9017-3_11).
- [15] M.F. Guerra, Da caracterização dos arqueometais, *Análise quantitativa por métodos nucleares e perinucleares*, Ph.D. Thesis Universidade Nova de Lisboa, Faculdade de Ciências e Tecnologia, 1990.
- [16] F.A. Magro, M.F. Guerra, J.-N. Barrandon, Les ceitis portugais (XVe–XVIe siècles): composition des alliages utilisés et problèmes numismatiques, *Revue Numismatique*, 6e Série – Tome 36 (1994), pp. 199–219, <https://doi.org/10.3406/numi.1994.2006>.

- [17] L.C. Alves, M.B.H. Breese, E. Alves, A. Paúl, M.R. da Silva, M.F. da Silva, J.C. Soares, Micron-scale analysis of SiC/SiC<sub>f</sub> composites using the new Lisbon nuclear microprobe, *Nucl. Instr. and Meth. in Phys. Res. B* 161–163 (2000) 334–338, [https://doi.org/10.1016/S0168-583X\(99\)00768-5](https://doi.org/10.1016/S0168-583X(99)00768-5).
- [18] G.W. Grime, M. Dawson, Recent developments in data acquisition and processing on the Oxford scanning proton microprobe, *Nucl. Instr. and Meth. in Phys. Res. B* 104 (1995) 107–113, [https://doi.org/10.1016/0168-583X\(95\)00401-7](https://doi.org/10.1016/0168-583X(95)00401-7).
- [19] J.A. Maxwell, W.J. Teesdale, J.L. Campbell, The Guelph PIXE software package II, *Nucl. Instr. and Meth. in Phys. Res. B* 95 (1995) 407–421, [https://doi.org/10.1016/0168-583X\(94\)00540-0](https://doi.org/10.1016/0168-583X(94)00540-0).
- [20] L. Robbiola, J.-M. Blengino, C. Fiaud, Morphology and mechanisms of formation of natural patinas on archaeological Cu–Sn alloys, *Corros. Sci.* 40 (12) (1998) 2083–2111, [https://doi.org/10.1016/S0010-938X\(98\)00096-1](https://doi.org/10.1016/S0010-938X(98)00096-1).
- [21] G. Masi, J. Esvan, C. Josse, C. Chiavari, E. Bernardi, C. Martini, M.C. Bignozzi, N. Gartner, T. Kosec, L. Robbiola, Characterization of typical patinas simulating bronze corrosion in outdoor conditions, *Mater. Chem. Phys.* 200 (2017) 308–321, <https://doi.org/10.1016/j.matchemphys.2017.07.091>.
- [22] E. Figueiredo, A Study on Metallurgy and Corrosion of Ancient Copper-based Artefacts from the Portuguese Territory, PhD thesis Universidade Nova de Lisboa, 2010, <http://hdl.handle.net/10362/5407>.